Defect Engineering in SiGe Heterostructures

H. Richter, A. Fischer, G. Kissinger, D. Krüger

Institute for Semiconductor Physics
Walter-Korsing-Str. 2, D-15230 Frankfurt (Oder), Germany

1. Introduction

The inter-relationships among semiconductor material, device fabrication process and device performance will continue to be the key to superior IC product performance, reliability and yield [1, 2]. From the point of view of semiconductor materials there are two ways to realize a high performance and yield in the semiconductor technology. The first way is the perfect crystal device technology, the as-grown state is widely preserved, and the second is the defect engineering. The first way is very expensive, cannot solve the problem of process-induced contamination with the increasing number of process-steps in advanced technologies. The second way "Defect Control" and "Defect Engineering" have become an important sector of modern semiconductor technology [2, 3]. Defect studies in semiconductor engineering started originally with seeking methods how to suppress generation of harmfull defects during device processing. Recently, the trend has appeared in witch defects are positively utilized to improve the device performance and reliability [4]. This plays a central role in stabilization, development of new processing steps, and tuning of special device parameters.

Defect engineering has acquired a form position in semiconductor technology, and not only in silicon-based electronics. There is a major importance when we try to approach the theoretical limits of semiconductor properties in practice.

Crystalline silicon and silicon-based materials such as silicon-germanium continue to be the primar material system. The driving technology towards higher integration densities is memory oriented. Today the new process lines are running with 200 mm Si wafers. CMOS is the king of technology, silicon is the king of materials [5]. At present, silicon-based technology is experiencing the transition to the next generation of substrates with a diameter of 300 mm [2, 6].

With the integration of heterostructures into the established silicon technology (a promising approach is the Si/Ge system) frequencies become attainable which used to be the exclusive domain of compound semiconductors. Heterostructures also make a reduction of the vertical device dimension possible. Therefore, they are well suited for advanced CMOS variants with lateral structures below 0.2 µm for fast integrated circuits. To understand the influence of new depostion methods, process-induced defects, metal contamination, and mechanical stress are a major task for present-day defect engineering. SiGe heterostructures with ultra thin layers and ultra sharp junctions promise a novel generation of silicon devices [7]. The growth of strained SiGe enables us to apply bandgap engineering to silicon-based devices (HBT, MODFET).

2. Misfit Strain Engineering in Heteroepitaxial Structures

The problems concerning the epitaxy of lattice-mismatched materials are well known. For sufficiently thin films the difference in the lattice constants leed to a pseudomorphically strained layer. In thicker films the strain within the layer is decreased by the generation of a dislocation network. Due to the lattice mismatch of 4.2 % in the SiGe system, strained $Si_{1-x}Ge_x$ layers exceeding the critical layer thickness, relax their stress via formation of misfit dislocations, their glessile threading parts intersecting the surface.

If the heteroepitaxial film is of a small lateral dimension, then the elastic stress relaxation, due to the boundary condition of zero traction at the edges, may be appreciable even at the center of the film pad. The

0-7803-3223-7/96/$5,00 © 1996 IEEE

TSMC 1018

Authorized licensed use limited to: Finnegan Henderson Farabow Garrett & Dunner. Downloaded on March 25,2024 at 22:19:16 UTC from IEEE Xplore. Restrictions apply.

strain energy density per unit area in a finite mesa will be smaller than that of an infinite layer. Any conceivable state of stress has three principal components. If one principal component is zero, we have the state of biaxial stress. Let us consider the principal components of biaxial stress $\sigma_1 = f(a)\,\sigma_x$ and $\sigma_2 = f(b)\,\sigma_x$. $f(a)$, $f(b)$ are functions of stress distribution along the orthogonal axes a, b. Far from any free surface, the stress state is uniformly biaxial of magnitude σ_x in both a and b in-plane directions. With approach to a free surface, the principal components very appreciably; the biaxiality of stress is changing from uniformly biaxial stress $\sigma_1 = \sigma_2 = \sigma_x$ at $f(a) = f(b) = 1$ to uniaxial loading $\sigma_1 = 0$, $\sigma_2 = \sigma_x$ or $\sigma_1 = \sigma_x$, $\sigma_2 = 0$ directly at a free surface at $f(a) = 0$, $f(b) = 1$ or $f(a) = 1$, $f(b) = 0$, respectively. Notice that a balanced biaxial stress remains for $f(a) = f(b) < 1$. Usually, elastic isotropy is assumed. Thus, the functions $f(a)$ and $f(b)$ must show the same structure. It has been shown by Reid [8] that, for in-plane strain, when dealing with deformation under combined stresses, a compound parameter called the effective stress is used which is related to a corresponding effective strain increment. The effective stress σ may be written in terms of the principal stresses of the biaxial stress state

$$\sigma = \{(1/2)\,[\sigma_1^2 + \sigma_2^2 + (\sigma_1 - \sigma_2)^2]\}^{1/2} \,. \tag{1}$$

σ is itself an invariant, and its value does not depend on the choice of coordinate axes. If the layer deforms with the substrate, the interface shear stresses acting on the potential slip systems are negligible. Putting the expressions for the principal components of biaxial compressive stress $\sigma_1 = f(a)\,\sigma_x$, $\sigma_2 = f(b)\,\sigma_x$ into Eq. (1), we get a general relation for the two-dimensional misfit stress distribution in mesa structures

$$\sigma = \sigma_x\,[\,f^2(a) + f^2(b) - f(a)\,f(b)\,]^{1/2} \,. \tag{2}$$

We can see that the effective stress σ approaches a local minimum when $f(a) \rightarrow 0.5\,f(b)$ or $f(b) \rightarrow 0.5\,f(a)$.

We are now going to consider how the function of stress distribution is structured in a patterned heteroepitaxial system. Previous analyses [9, 10] of the film stress σ_f at the edges of multilayer structures have been based on the simplifying assumption of a line force concentrated at the film edge tangential to the substrate surface, giving a step-function stress distribution $\sigma_f = \sigma_x$ within the film and $\sigma_f = 0$ at the film edge. This stress distribution which is only valid for an infinitely rigid substrate was modified by Hu [11] by allowing the surface film to deform with the substrate. In his model a relaxing film stress σ_f is zero at the film edge and then rises asymptotically towards its maximum value σ_x as a function of the distance from the edge. A measure for the film stress relaxation near an edge is given by the relative rigidity K between the substrate and the layer which can be written as a plate modulus ratio of the substrate and film materials $K = \mu_s(1-\nu_f^2)/\mu_f(1-\nu_s^2)$, where μ denotes Young's modulus, ν is the Poisson's ratio, and the subscripts s and f refer to the substrate and the film, respectively. Hu's analysis leads to an integral equation for the film stress distribution which can only be solved numerically. To obtain an analytical close expression for the zero traction at the edges, we fitted an exponential function to the numerical values [11] using the substrate-to-film rigidity ratio K as a parameter. In the K-range of practical relevance, the following relation for the film stress relaxation due to the creation of a film edge can be given [12]

$$\sigma_f = \sigma_x\,\{1 - \exp[-(2Ka/\pi h)^{1/2}]\}, \tag{3}$$

where a is the orthogonal distance from the film edge and h is the film thickness. It should be mentioned that Eq. (3) represents a good approximation of the numerical solution of Hu's integral equation and now makes it possible to analyse the biaxial stress problem of a patterned layer structure on substrate.

Authorized licensed use limited to: Finnegan Henderson Farabow Garrett & Dunner. Downloaded on March 25,2024 at 22:19:16 UTC from IEEE Xplore. Restrictions apply.

So far we have been considering stress relaxation near a single film edge. The general result is presented in Fig. 1 (a), (b).

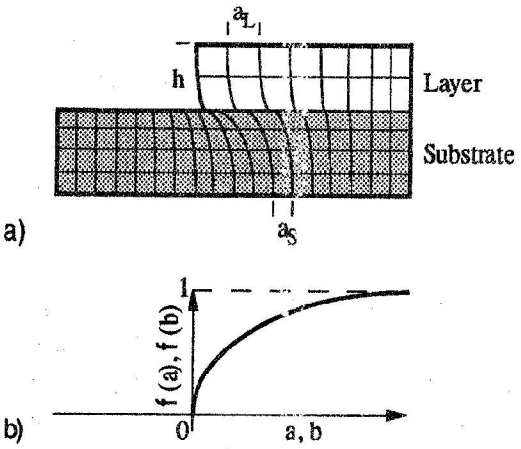

Fig. 1. Schematic diagrams showing (a) a single edge of a heteroepitaxial layer structure on substrate (h is the layer thickness and a_L, a_S represent the lattice constants of the layer and substrate material, respectively) and (b) the corresponding orthogonal components of stress distribution f (a), f (b) in the film versus distances a, b from a film edge.

Imagine now a second infinitely long edge lying parallel in opposite direction to the first one at a distance of A. Substituting into Eq. (3) (A-a) for a, we get the film stress distribution σ_f' near the second edge

$$\sigma_f' = \sigma_x (1 - \exp\{-[2K(A-a)/\pi h]^{1/2}\}) . \qquad (4)$$

According to the principle of superposition, we combine the last two Eqs. (3) and (4) and get a uniaxial misfit stress distribution produced by a double edge. Applying this result to the previous equation $\sigma_1 = f(a)\ \sigma_x$, the function of stress distribution along the axis a becomes [13]

$$f(a) = 1-\exp[-(2Ka/\pi h)^{1/2}] - \exp\{-[2K(A-a)/\pi h]^{1/2}\}. \quad (5)$$

In the same manner the distribution of the principal stress $\sigma_2 = f(b)\ \sigma_x$ along the axis b between two edges having a distance of B to each other will be simply

$$f(b) = 1-\exp[-(2Kb/\pi h)^{1/2}]-\exp\{-[2K(B-b)/\pi h]^{1/2}\}. \quad (6)$$

Using these orthogonal components of stress distribution in Eq. (2), the effective stress σ of the biaxial stress state of a rectangular mesa structure A·B·h on substrate is obtained. The boundary conditions of Eqs. (5) and (6) are $0 \le a,b \le A, B$ and $0 \le f(a), f(b) \le 1$. Two limiting cases are readily apparent from Eqs. (2), (5), and (6). They are: $\sigma = \sigma_x$ for $K \to \infty$ or (A or B) $\to \infty$ and $\sigma = 0$ for $K \to 0$ or (A and B) $\to 0$. To summarize, then, the expressions (2), (5), and (6) are very useful. They allow us to predict the alteration of misfit stress values in dependence on material and size characteristics of the patterned heteroepitaxial layer-substrate system.

So far we have been considering elastic misfit stress relaxation in a monolayer mesa structure on infinite substrate. Imagine now a second thin layer of thickness H lying between the strained film and the bulk material, e. g. a buffer layer, and that the left half of the bilayer system is severed from the substrate. It allows the multilayered coating of thickness (h+H) as a whole to deform with the substrate, as illustrated in Fig. 2 (a), (b). This means that for a bilayer mesa structure studied here, the underlying layer H acting as a partial free-standing substrate for the strained layer pad becomes apparently softer. Obviously, the effective rigidity ratio of the patterned substrate and the strained layer diminishes as the thickness of the underlying layer increases. Considering the bilayer-on-substrate structure to be two elastic systems acting independent upon one another, we get the new measure for the effective film stress relaxation: $[(h+H)/K]_{eff} = h/K_h+H/K_H$, where K_h is the relative rigidity between the patterned underlying layer H and the upper layer h, and K_H is the relative rigidity between the infinite substrate and the patterned underlying layer H. For our vertical structure - strained layer / substrate buffer layer / substrate - where $K_H = 1$, the term $[K/(h+H)]_{eff}$ is equal to $K_h/(h+K_hH)$. To consider the effect of patterned substrate structures on elastic strain relaxation, we replace the value K/h by the term K/(h+KH) in Eqs. (5) and (6). (For simplicity, the value K_h is represented as K.)

Authorized licensed use limited to: Finnegan Henderson Farabow Garrett & Dunner. Downloaded on March 25,2024 at 22:19:16 UTC from IEEE Xplore. Restrictions apply.

Now the orthogonal components of stress distribution can be written as

$$f(a) = 1 - \exp\{-[2Ka/\pi(h+KH)]^{1/2}\} - \exp\{-[2K(A-a)/\pi(h+KH)]^{1/2}\}, \quad (7)$$

$$f(b) = 1 - \exp\{-[2Kb/\pi(h+KH)]^{1/2}\} - \exp\{-[2K(B-b)/\pi(h+KH)]^{1/2}\}. \quad (8)$$

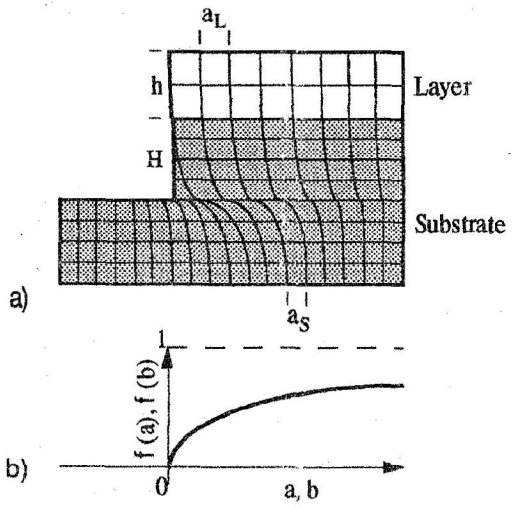

Fig. 2. Schematic diagrams showing (a) a single edge of a bilayer structure on substrate (h is the layer thickness, H is the underlying layer thickness, and a_L, a_S represent the lattice constants of the layer and substrate material, respectively) and (b) the corresponding orthogonal components of stress distribution f (a), f (b) in the film versus distances a, b from a film edge.

Fig. 2(b) shows how these functions of stress distribution differ from the first ones for a monolayer edge system represented in Fig. 1(b). Notice that the former distribution functions (5) and (6) represent a special case of the functions (7) and (8) for H = 0. Let us now take stock: For heteroepitaxial mesa structures on unpatterned substrate, the strain is predominantly in the epitaxial thin film because the substrate is too rigid to be compliant. For small substrate islands, the strain energy is more evenly distributed between the epilayer and the substrate material so that the strain energy density per unit area is reduced.

Using the new orthogonal components of stress distribution in Eq. (2), the effective stress σ of the biaxial stress state of a multilayered rectangular mesa structure A·B·(h+H) on substrate is obtained. The boundary conditions of Eqs. (7) and (8) are $0 \le a,b \le A, B$ and $0 \le f(a), f(b) \le 1$. Two limiting cases are readily apparent from Eqs. (2), (7), and (8). They are: $\sigma = \sigma_x$ for (A or B) $\to \infty$ and $\sigma = 0$ for (A and B) $\to$ The application of our stress analysis will now be discussed briefly. Take the case of $K \approx 0.8$ for the substrate/layer systems Si/SiGe, Ge/Si, or InP/GaAs. The results of the residual elastic stress calculation are shown in Figs. 3 and 4 for relaxation via strained layer mesa structure on unpatterned substrate of the size A·B·h and strained layer mesa structure on patterned substrate of the size A·B·(h+H), respectively.

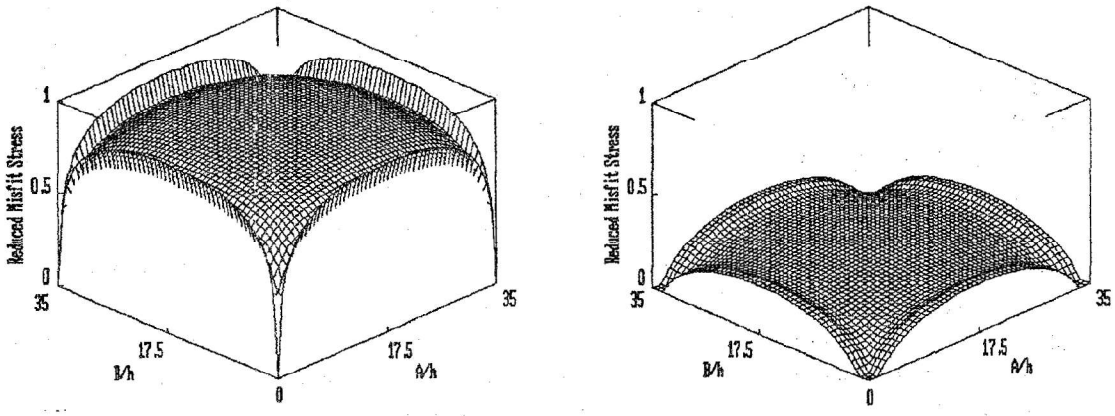

Fig. 3 and 4 Plot of reduced misfit stress σ/σ_x vs A/h = 35, B/h = 35 for the case K = 0.8, Fig. 3 H = 0 and Fig. 4: H = 10 h

Authorized licensed use limited to: Finnegan Henderson Farabow Garrett & Dunner. Downloaded on March 25,2024 at 22:19:16 UTC from IEEE Xplore. Restrictions apply.

To simplify matters the effective stress σ reduced to the ratio σ/σ_x is plotted versus the normalized mesa sizes A/h and B/h. From Fig. 3, it is seen that the misfit stress is hardly relaxed in mesa structures on infinite substrate. However, Fig. 4 shows the intense stress relaxation expected from strained layer mesa structure on patterned substrate. Here it is obvious that, at a given epilayer thickness, the strain energy density per unit area in a patterned lattice-mismatched heterostructure is appreciably lower than that of a strained layer mesa structure lying immediately on an infinite substrate.

3. Deformation Behaviour of Strained Layer Heterostructures

To demonstrate the physical significance of our new approach in equilibrium theory for strained layer relaxation [14], we have calculated the equilibrium critical thickness of $Si_{1-x}Ge_x/Si$ strained layers as a function of the fractional atomic Ge content x and compared our results with those predicted by classical relaxation models, which do not include surface relaxation effects. Taking the in-plane misfit strain $\varepsilon = 0.0418x$ and the equilibrium conditions for the point of strain relief onset via plastic flow, i.e., $\tau_{exc} = 0$ and misfit dislocation spacing $p \rightarrow \infty$, leads to the following expression for the critical thickness h_{crit}:

$$\frac{b\cos\lambda}{0.0836\, h_{crit}}\left[1 + \frac{\frac{1-\nu}{4}}{4\pi\cos^2\lambda\cos\phi\,(1+\nu)}\ln\frac{h_{crit}}{b}\right] \qquad (9)$$

In the absence of surface relaxation forces, the equilibrium critical thickness of a single strained epilayer upon a substrate of different lattice parameter according to Matthews and Blakeslee is given by the formulation reported in reference [8]. Inserting appropriate material parameters in Eq. (9) and in the MB formulation, $\cos\lambda = 0.5$, $\cos\phi = 0.816$, $\nu = 0.278$, and $b = 3.84$ Å for growth on (001) surface, the critical thickness calculated for the two different models are plotted in Fig. 5. It is seen, at first glance, that our values of h_{crit} represented by Eq. (9) are much larger than the values calculated using equation of MB. Moreover, for a fractional atomic Ge content x greater than 0.5, the MB formulation does not provide any value for h_{crit}. Additionally, we have compared our theoretical results with the published experimental data [16,17] of h_{crit} obtained from $Si_{1-x}Ge_x/Si$ structures, grown by molecular beam epitaxy at a growth temperature of 750 °C. For each composition, there is good agreement between our theoretical results and experimental data reported in [16 and 17]. For example, for $x = 0.25$, h_{crit} was found to be approximately 200 Å. As seen in Fig. 5, for this case, our analysis yields the value of 200 Å. The MB model predicts only an equilibrium critical thickness value of 60Å.

Let us now consider film stresses for elastically strained $Si_{1-x}Ge_x/Si$ layers. For the pseudomorphically strained layer case, where $p \rightarrow \infty$, the in-plane film stress σ becomes:

$$\sigma = \frac{2G(1+\nu)}{1-\nu}\left(0.0418\,x - \frac{b\cos\lambda}{2h}\right) \qquad (10)$$

This equation can then be used to predict the stress response to a strain increment, which is related to the volume change of the layer. The first term on the right-hand side corresponds to a volume expansion due to Ge incorporation and the second one to a volume contraction via surface relaxation. Thus, the residual in-plane strain is given by $\varepsilon = 0.0418x\text{-}(b\cos\lambda/2h)$. For thin layers, this relation is essential for experimental determination of x as a function of the tetragonal distortion of the cubic lattice cells. Figure 6 shows a plot of σ vs h for $x = 0.3$, $G = 51$ GPa. This relation has been studied experimentally too. The in-plane epitaxial film stress σ as a function of layer thickness was measured in a *Thin Film Stress Measuring Apparatus*. In Fig. 6, our experimental data are also shown. It is seen that there is good agreement between our theoretical results and experimental data. This tells us that the elastic coherency stress of the strained material in the plane of the

Authorized licensed use limited to: Finnegan Henderson Farabow Garrett & Dunner. Downloaded on March 25,2024 at 22:19:16 UTC from IEEE Xplore. Restrictions apply.

surface is really affected by a large surface relaxation stress. Consequently, calculations of the Ge composition x for SiGe epitaxy based only on misfit strain values assuming bulk lattice spacings could be seriously in error.

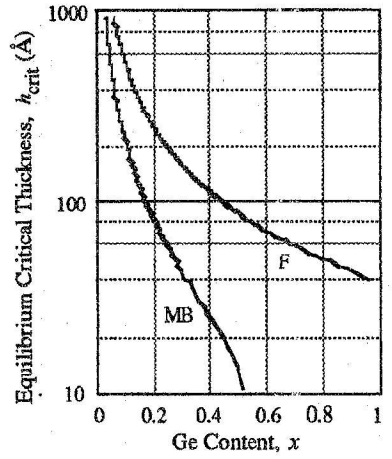

Fig. 5. h_{crit} vs x for different relaxation models; non-stress-free body (MB), stress-free body (F: this study).

Finally, we will examine the plastic flow, work hardening, and the degree of strain relaxation in $Si_{1-x}Ge_x/Si$ layers. The in-plane film stress σ becomes:

$$\sigma = \frac{2\,G\,(1+\nu)}{1-\nu}\left(0.0418\,x - \frac{b\cos\lambda_t}{2R_{h,p}}\right) \qquad (11)$$

Putting the values of the material parameters into Eq. (11), assuming a metastable epilayer with $x = 0.3$ and $h = 500$ Å, we can evaluate the variation in excess resolved shear stress [14] acting on the slip system τ_{exc} and epitaxial film stress σ for the complete thermal relaxation process. At the beginning of deformation, where $p \rightarrow \infty$, $\tau_{exc} = 0.7$ GPa and $\sigma = 1.9$ GPa, as illustrated in Fig. 7. During plastic flow via dislocation generation and propagation, τ_{exc} and σ diminish continuously and then remain unchanged at zero and 1.15 GPa, respectively, whereas the shear self-stress component τ_s rises to its maximum value. At this equilibrium deformation stage, the applied misfit stress and the shear component of elastic stress field due to dislocation interaction compensate one another and strain relief via plastic flow comes to rest. Thus, as a result of work hardening, the lattice mismatched epilayer will remain in a certain state of strain at the end of relaxation process.

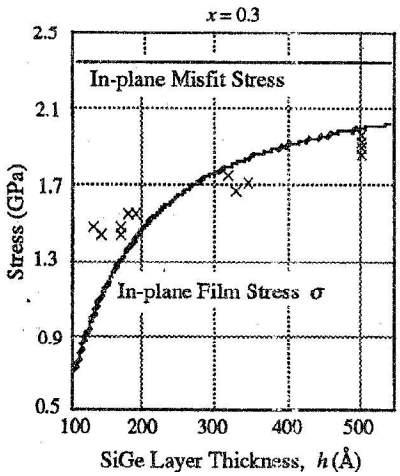

Fig. 6. Theoretical (solid line) and experimental (×) film stress σ vs h.

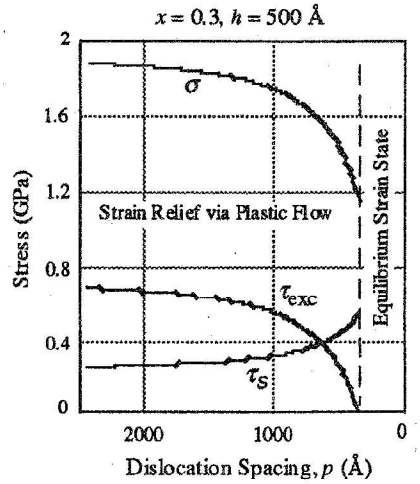

Fig. 7. Decrease in film stress σ and excess shear stress τ_{exc} during plastic flow as a function of spacing p.

4. Stepwise Equilibrated Graded Buffers

An essential requirement for n-type modulation doped Si/SiGe structures is a Si-channel being under tensile strain. Strain-relaxed compositionally graded buffers provide a possibility to adjust the lattice constant of a Si or Ge substrate wafer to any value between these two elements. In this way a tensile strained Si channel can grow on a totally relaxed virtual SiGe substrate. The major problem of these totally relaxed heterostructures are threading dislocations (TDs). Due to the lattice mismatch of 4.2 % in the Si-Ge system, strained

Authorized licensed use limited to: Finnegan Henderson Farabow Garrett & Dunner. Downloaded on March 25,2024 at 22:19:16 UTC from IEEE Xplore. Restrictions apply.

layers exceeding the x-dependent critical layer thickness relax their stress via formation of misfit dislocations. Their glissile threading parts intersecting the surface are detrimental to transport properties of modulation-doped structures [18]. Usually, TD densities between 10^4 and 10^6 cm^{-2} have been obtained in compositionally graded buffer layers [18 - 25]. However, all these methods to grow unstrained $Si_{1-x}Ge_x$ buffers operate without adjustment of equilibrium conditions for stress relaxation. In our experiments stepwise equilibrated graded buffers on Si were grown by APCVD with TD densities in the 10^2 to 10^3 cm^{-2} range [26]. These buffer layers were grown stepwise with a layer by layer increasing Ge concentration. After each layer the growth process was stopped in order to achieve a nearly complete stress relaxation during an in-situ anneal at temperatures $\geq$ 1000 °C. In this way each layer of the buffer is grown on a relaxed alloy layer.

Stepwise equilibrated graded buffers were grown on 4 in. (001) boron-doped FZ silicon and CZ silicon wafers with resistivities of 6-8 Ωcm and 1000 Ωcm (only FZ) in order to study the influence of the substrate material. The ideal step width is 5 % Ge, however, deviations of ± 3 % Ge of the step width are possible. In this way 4-step and 5-step buffers were grown capped with a 300nm thick layer of the same concentration as the upper buffer layer containing 23 % Ge and 28 % Ge, respectively. Each and every layer deposition was followed by an in-situ anneal in hydrogen at 1050 °C usually for 1hour.

Owing to the extreme low density of TDs their density was counted by interference phase contrast microscopy after etching the surface with a diluted Yang etchant [27]. The equilibrating in-situ anneal after each layer requires extended periods of time as demonstrated in [28]. It is shown that the first half of misfit strain is relaxed in less than 5 min. In contrast, the relaxation of the residual strain needs more than 1 h. Especially, all the dislocations that have not reached the opposite wafer edge are responsible for the TD density in the cap layer. Most of the gliding TDs are nucleated at the wafer edge. Detailed investigations concerning the annealing time dependence during growth of 4-step buffers have shown that 1 h of equilibration at 1050 °C is needed in order to achieve really low TD densities of 10^2 to 10^3 cm^{-2} [16]. The silicon substrate material has an important influence on the quality of the cap layer. It is impossible to grow buffers with low TD densities on CZ silicon because to much sources of dislocations exist in the substrate that cause an uncontrolled nucleation of extra TDs. Also the resistivity of FZ silicon has an influence on the processing conditions. The upper temperature for the equilibrating heat treatments is limited by slips in the substrate also leading to uncontrolled dislocation nucleation [26]. The higher the resistivity the lower the highest possible annealing temperature. For 6-8 Ωcm and 1000 Ωcm FZ silicon equilibration annealings at 1050 °C and 1020 °C, respectively, are possible. However, the lower the annealing temperature the longer the equilibration needs because the glide velocity is decreasing with decreasing temperature. Therefore, 1000 Ωcm wafers require 1.25 h equilibration annealings instead of 1h used for 6-8 Ωcm material.

TEM studies [28] of the dislocation network after in-situ annealing of the first buffer layer have shown that 60° and 90° dislocations are present. With increasing annealing periods more and more misfit dislocations bend off the <110> directions first to <100> directions and later to some other directions. It is believed that this is due to interdiffusion which remarkably influences the relaxation process at such high temperatures. In

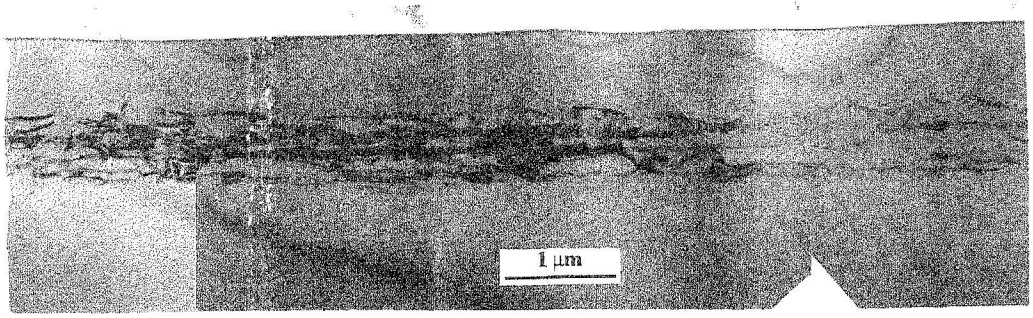

Fig. 8: TEM cross-sectional micrograph of a 5-step buffer with equilibration annealings at 1050 °C for 1 h and 28 % Ge in the cap layer

Authorized licensed use limited to: Finnegan Henderson Farabow Garrett & Dunner. Downloaded on March 25,2024 at 22:19:16 UTC from IEEE Xplore. Restrictions apply.

the beginning dislocations are also emitted into the substrate. They connect the dislocation networks between the buffer steps and at least a threedimensional network is formed in the finished buffer as seen in Fig. 8. Above this network exists a perfectly grown layer almost free of TDs.

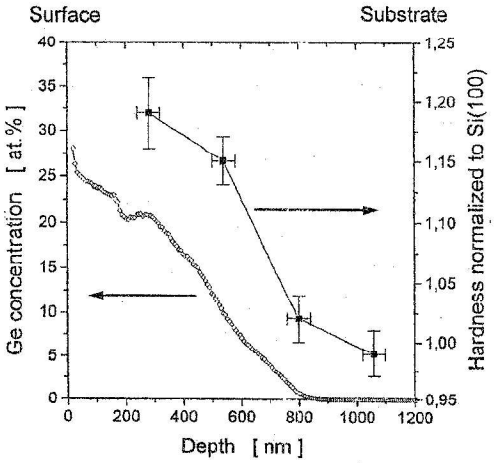

Fig. 9: Ge-Profile and hardness of a bevelled SiGe buffer

Secondary ion mass spectrometry (SIMS) measurements have shown that the step grading was smoothed during the in-situ anneals [29]. The profile of the Ge concentration bears a great resemblance to continuously graded buffers shown in Fig. 9. This graph additionally contains the hardness profile on the buffer. The hardness is increasing with Ge concentration.

It was shown that equilibration annealings at temperatures > 1000 °C are an effective way to reduce the threading dislocation density in the cap layer of Ge_XSi_{1-X} buffers to values lower than 10^3 cm^{-2}. In this way relaxed buffer layers of high thermal stability are attainable. The temperature and duration of the equilibration annealings depend on the resistivity of the FZ silicon.

5. Optimal Doping Concentration Profiles and Influence of non-equilibrium Point Defects

One of the most important requirements for profile and defect engineering is to obtain and to keep the optimal dopant concentration profiles in HBT structures. Process induced point defects are one reason which can significantly influence these profiles. A principal composition and doping profile for a HBT with high transit frequencies f_T is shown schematically in Fig. 10.

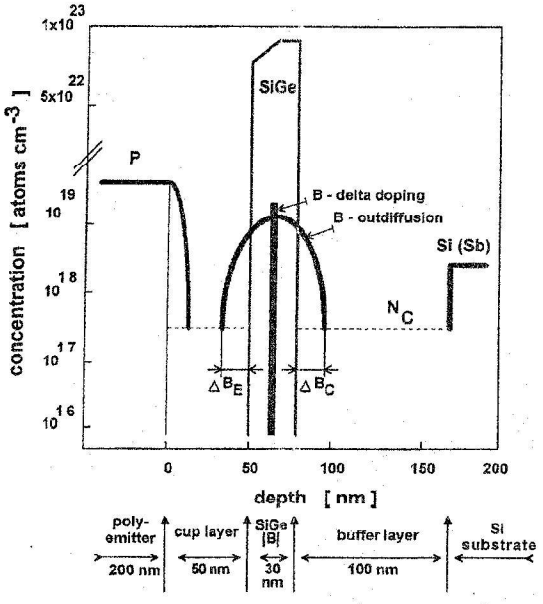

Fig. 10: Vertical composition and doping profil (schematic) for a HBT structure with high transit frequencies f_T

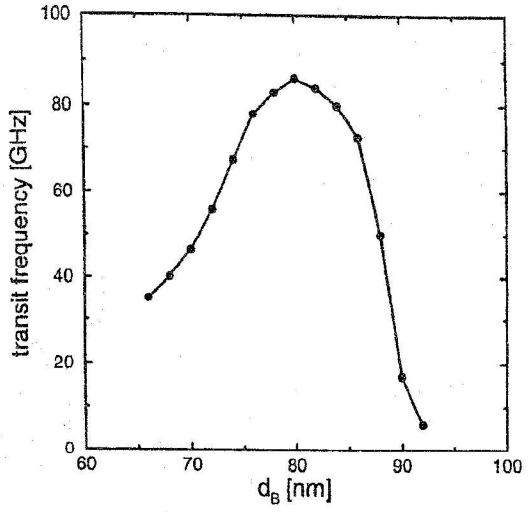

Fig. 11: Simulated transit frequency at optimum current vs position of the B peak

Authorized licensed use limited to: Finnegan Henderson Farabow Garrett & Dunner. Downloaded on March 25,2024 at 22:19:16 UTC from IEEE Xplore. Restrictions apply.

In this profile a sharp B doped area (in the given case delta-like) is located within a 30 nm $Si_{1-x}Ge_x$ layer with a graded Ge profile, increasing from about 5 at. % to about 20 at. %, over a distance of about 20 nm, followed by an about 10 nm region with constant Ge level of 20 at. %. The emitter is formed by ultra-shallow out-diffusion from a highly doped layer of about 150 nm poly-Si with a diffusion length into the Si substrate of less than 50 nm. The collector, grown on a Sb-doped substrate, is doped with Sb during the MBE growth.

As visible from Fig. 10, the heterostructure is characterized by ultra-shallow junctions located inside different materials. However, the situation becomes even more complicated as a result of technological processing of the grown structure. One important feature is the possible B out-diffusion from the $Si_{1-x}Ge_x$ layer, as shown schematically in Fig. 10. Out-diffusion of B towards the emitter (ΔB_E) of only a few nm reduces f_T significantly, and the same holds for out-diffusion towards the collector. Boron is generally supposed to diffuse in a silicon crystal predominantly by a mechanism that involves Si self-interstitials. Thus, the interstitial part of its diffusivity at a particular point in a Si lattice depends on the interstitial concentration in that point.

The out-diffusion of the B at the emitter side results in an electric counter field in the Si part of the base since the field from the steep rising boron profile is no longer compensated by that from the graded Ge profile. On the other hand, out-diffusion at the collector side results in a strong counter field produced by the decline of the Ge concentration within the base which is no longer compensated by the electric field of the space-charge region. Both of these effects reduce current gain and the transit frequency drastically and make the transistor useless for high-speed applications.

In [30] B profiles of the same dose but of different shape and position were investigated numerically. In order to demonstrate the position dependence of f_T the B peak was moved from its optimum position (d_B=80nm) towards the emitter and the collector respectively. Again, for each position the transit frequency f_T at optimum collector current was calculated. The results are represented in Fig. 11

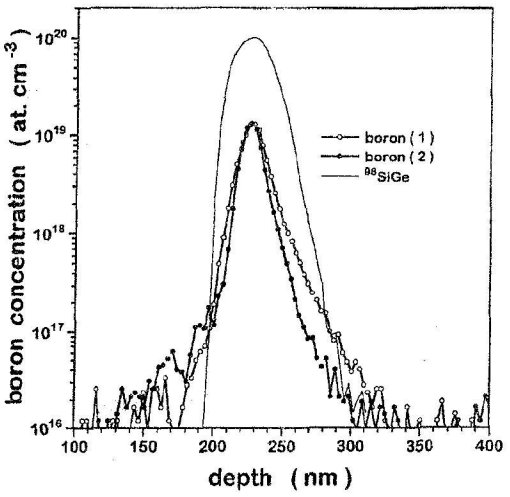

Fig. 12 SIMS depth profiles indicating increased B out-diffusion in SiGe layers into a high doped As sub-collector (curve 1) in comparision to a Sb doped sub-collector (curve 2).

We observe a drastic reduction of f_T produced by a doping shift of a few nanometers, especially at the collector side. We conclude that an accurate knowledge about shape and position is of the doping pro-file is required for device and defect engineering. It is desirable to measure the doping profiles of the HBT structure with a depth resolution in the range of 3 to 5 nm, to characterize quantitatively the Ge concentration and the gradient in the base area of about 30 nm, and the relative position of B in the base. The measurement of B out-diffusion is closely related to the optimization of the technological process since it allows an estimate to be made of the upper limit of the temperature-time budget and critical steps from the position of point defect injection.

Figure 12 shows an example for increased out-diffusion of B in a HBT structure due to non-equilibrium point defect injection (Si self interstitials) from a high concentration implanted As sub-collector (curve1) in comparison to a lower doped Sb sub-collector (curve 2) processed under the same conditions.

ACKNOWLEDGEMENT

The author wish to thank their collegues of the Institute of Semiconductor Physics who contributed to this results and the collegues of the project team of Dr. Hersener (Daimler-Benz-AG, Research Center Ulm) for their valuable discussions and financial support.

Authorized licensed use limited to: Finnegan Henderson Farabow Garrett & Dunner. Downloaded on March 25,2024 at 22:19:16 UTC from IEEE Xplore. Restrictions apply.

REFERENCES

1 H. Richter, M. Mai, F. Kirscht, P. Gaworzewski, Physica 116 B (1993) 162

2 H. Huff, Proc. of the Fourth International Symposium on ULSI, 103 (1993), ECS, and Proc. GADEST '95, Solid State **47 - 48**, 65 (1996)

3 H. Richter et al., Proc. "Gettering and Defect Engineering in Semiconductor Technolog - GADEST" 1985, 1987, 1991, 1993, 1995

4 J. Chikawa, K. Sumino, K. Wada, "Defects and Properties of Semiconductors: Defect Engineering", KTK Scientific Publ. 1987

5 National Technology Roadmap for Semiconductors, SIA, San Jose, Nov. 1994

6 W. v. Ammon, Solid State Phenomena **47 - 48**, 97 (1996)

7 U. König, J. Hersener, Solid State Phenomena **47-48**, 17 (1994)

8 C. N. Reid, *Deformation Geometry for Materials Scientists* (Pergamon, Oxford, 1973)

9 E. S. Meieran and I. A. Blech, *J. Appl. Phys.* **36**, 3162 (1965).

10 S. M. Hu, *Appl. Phys. Lett.* **32**, 5 (1978).

11 S. M. Hu, *J. Appl. Phys.* **50**, 4661 (1979).

12 A. Fischer, *Cryst. Res. Technol.* **18**, 1415 (1983).

13 A. Fischer and H. Richter, *Appl. Phys. Lett.* **61**, 2656 (1992).

14 A. Fischer, H. Kühne and H. Richter, *Phys. Rev. Lett.* **73**, 2712 (1994).

15 J. W. Matthews and A. E. Blakeslee, *J. Cryst. Growth* **27**, 118 (1974) and **32**, 265 (1976).

16 E. Kasper, in *Physics and Applications of Quantum Wells and Superlattices*, E. E. Mendez and K. von Klitzing, Plenum Press, New York and London, 1987, p.101.

17 R. People and J. C. Bean, *Appl. Phys. Lett.* **47**, 322 (1985).

18 K. Ismail, F. K. LeGoues, K. L. Saenger, M. Arafa, J. O. Chu, P. M. Mooney, and B. S. Meyerson, Phys. Rev. Lett. **73**, 3447 (1994).

19 E. A. Fitzgerald, Y. H. Xie, M. L. Green, D. Brasen, A. R. Kortan, J. Michel, Y. J. Mii, and B. E. Weir, Appl. Phys. Lett. **59**, 811 (1991).

20 J. W. P. Hsu, E. A. Fitzgerald, Y. H. Xie, P. J. Silverman, and M. J. Cardillo, Appl. Phys. Lett. **61**, 1293 (1992).

21 Y. H. Xie, E. A. Fitzgerald, D. Monroe, P. J. Silverman, G. P. Watson, J. Appl. Phys. **73**, 8364 (1993).

22 G. P. Watson, E. A. Fitzgerald, Y. H. Xie, and D. Monroe, J. Appl. Phys. **75**, 263 (1994).

23 F. K. LeGoues, B. S. Meyerson, and J. F. Morar, Phys. Rev. Lett. **66**, 2903 (1991).

24 K. Ismail, B. S. Meyerson, and P. J. Wang, Appl. Phys. Lett. **58**, 2117 (1991).

25 F. K. LeGoues, B. S. Meyerson, J. F. Morar, and P. D. Kirchner, J. Appl. Phys. **71**, 4230 (1992).

26 G. Kissinger, T. Morgenstern, G. Morgenstern, and H. Richter, Appl. Phys. Lett. **66**, 2083 (1995).

27 K. H. Yang, J. Electrochem. Soc. **131**, 1140 (1984).

28 G. Kissinger, T. Morgenstern, H. B. Erzgräber, G. Morgenstern, G. G. Fischer, W. Kissinger, and H. Richter, Electrochem. Soc. Proc. Vol., **96-5**, 366 (1996).

29 G. Kissinger, T. Morgenstern, G. Morgenstern, H. B. Erzgräber, and H. Richter, Mat. Res. Soc. Symp. Proc. Vol. **378**, 141 (1995).

30 D. Krüger, R. Kurps, B. Heinemann, F. Herzel, H. P. Zeindl, J. Vac. Sci. Techn., **B14**, 287 (1996)

Authorized licensed use limited to: Finnegan Henderson Farabow Garrett & Dunner. Downloaded on March 25,2024 at 22:19:16 UTC from IEEE Xplore. Restrictions apply.